RSC Advances

PAPER

View Article Online
View Journal | View Issue

Cite this: *RSC Adv.*, 2021, **11**, 15323

BSA-encapsulated cyclometalated iridium complexes as nano-photosensitizers for photodynamic therapy of tumor cells†

Yao Xu, Xiang Wang, Kang Song, Jun Du, Jinliang Liu, Yuqing Miao and Yuhao Li*

Received 5th March 2021
Accepted 16th April 2021

DOI: 10.1039/d1ra01740c

rsc.li/rsc-advances

Photodynamic therapy is a promising treatment method. The development of suitable photosensitizers can improve therapeutic efficacy. Herein, we report three iridium complexes (**Ir1**, **Ir2**, and **Ir3**), and encapsulate them within bovine serum albumin (BSA) to form nano-photosensitizers (**Ir1**@BSA, **Ir2**@BSA, and **Ir3**@BSA) for photodynamic therapy (PDT) of tumor cells. In the structures of Ir(III) complexes, we use the pyrazine heterocycle as part of the C^N ligands and explore the effect of different ligands on the ability to generate singlet oxygen ($^1O_2$) by changing the conjugation length of the ligand and increasing the coplanarity of the ligand. Besides, the fabricated nano-photosensitizers are beneficial to improve water dispersibility and increase cellular uptake ability. Through studying photophysical properties, $^1O_2$ generation capacity, and cellular uptake performance, the results show that **Ir1**@BSA has the best photodynamic therapeutic effect on 4T1 tumor cells. This study provides an effective research basis for the further design of new nano-photosensitizers.

Introduction

Photodynamic therapy (PDT) is a noninvasive, photo-controlled treatment method.[1–4] Based on the generation of photo-induced reactive oxygen species (ROS), this method has been widely utilized in cancer treatment such as for bladder cancer, esophageal cancer, lung cancer, and brain cancer, exhibiting some superiorities over traditional cancer treatments including operative treatment, radiotherapy, and chemotherapy.[5–9] Three factors influence the effectiveness of PDT including photosensitizer, oxygen, and light.[10] Through producing more ROS to obtain a better therapeutic effect, the researchers have started from these three factors and designed multiple methods to enhance PDT. For example, the nanomaterial is used to carry oxygen to supply raw materials for PDT.[11–14] For another example, the structure of the photosensitizer is adjusted to increase singlet oxygen quantum yield.[15–18] Besides, the excitation light is regulated to increase the penetration depth of the light into the tissue for internal tumor treatment.[19,20]

Numerous studies have shown that among the three factors, designing novel photosensitizers through structural optimization strategies is a feasible and effective way to enhance the therapeutic effect.[21–24] Benefit from the development of chemical synthesis, many types of photosensitizers have been developed. Among them, noble metal complex photosensitizers have attracted great attention, such as ruthenium complexes,[25,26] platinum complexes,[27,28] iridium complexes,[29,30] *etc.* Iridium Ir(III) complexes possess higher intersystem crossing efficiency and better photobleaching resistance than some organic photosensitizers. More specifically, Ir(III) complexes show a triplet excited-state lifetime from nanosecond to microsecond, beneficial for the energy transfer to react with $^3O_2$ to generate $^1O_2$.[31] For heteroleptic cationic Ir(III) complexes, through adjusting their cyclometalated ligands (C^N ligand) and ancillary ligands (N^N ligand), the ground state absorption and excited-state absorption of the complexes are regulated to achieve effective triplet energy transfer, and ultimately increase singlet oxygen quantum yield.[32,33] Although some studies have been focused on the relationship between ligand and singlet oxygen quantum yield, and some Ir(III) complexes have been synthesized based on the modification of C^N ligand and N^N ligand, there is still no clear enunciation for the structure–activity relationship between them.

Besides, most Ir(III) complexes are water-insoluble. To make these Ir(III) complexes become photosensitizers for biological application, it is necessary to overcome the problem of insufficient water solubility. There are two methods to solve this problem. One way is to introduce hydrophilic groups or water-soluble polymers into an Ir(III) complex by covalent bonding to improve the solubility.[34–36] Another way is to utilize biocompatible polymers or protein to encapsulate the Ir(III) complex to improve the water dispersibility.[37,38] These two strategies provide strategies for the further application of Ir(III) complexes as photosensitizers.

Institute of Bismuth Science, College of Science, University of Shanghai for Science and Technology, Shanghai 200093, China. E-mail: yhli@usst.edu.cn

† Electronic supplementary information (ESI) available. See DOI: 10.1039/d1ra01740c

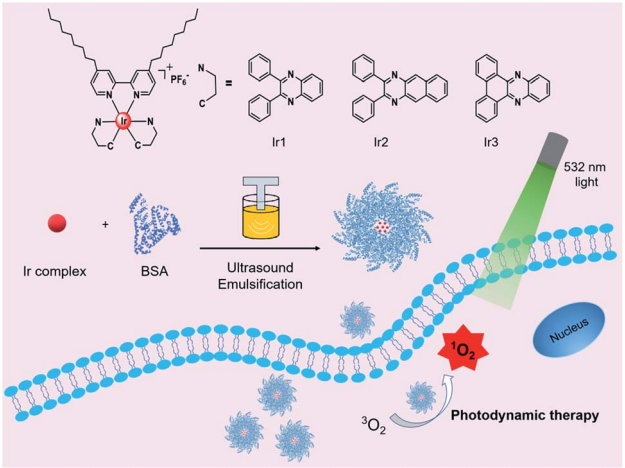

Scheme 1 Molecular structures of **Ir1** to **Ir3** complexes and schematic of **Ir1**@BSA to **Ir3**@BSA, fabrication, and application for photodynamic therapy.

Herein, we reported a series of three bovine serum albumin (BSA)-encapsulated Ir(III)-based nano-photosensitizers (**Ir1**@BSA, **Ir2**@BSA, and **Ir3**@BSA) for photodynamic therapy of tumor cells. The three iridium complexes (**Ir1** to **Ir3**) possess different C^N ligands. Based on the 2,3-diphenylquinoxaline structure in **Ir1**, introduce a benzene ring to extend the conjugation length of C^N ligand in **Ir2** or connect the two phenyl groups to construct a more plane-rigid C^N ligand in **Ir3** to explore the relationship between these influencing factors and singlet oxygen generation ability. Also, to increase the water dispersibility, we encapsulated BSA on the surface of the synthesized complexes by self-assembly to construct nano-photosensitizers. Introducing two long alkyl chains into the N^N ligand would make an Ir(III) complex that could be better embedded in the hydrophobic cavity of BSA during self-assembly to achieve a tighter combination. The study of three protein-encapsulated nano-photosensitizers could provide a research foundation with exploring Ir(III) complexes for photodynamic therapy (Scheme 1).

Results and discussion

Synthesis

The synthesis route from **Ir1** to **Ir3** was shown in Fig. S1.† These iridium complexes were synthesized in a three-step method. To begin with, three pyrazine derivatives (dpqx, dpbq, and dbpz) were synthesized through the reaction of dehydration between diketones and diamine compounds. Subsequently, the dimeric iridium complexes were obtained from the reaction between these ligands and $IrCl_3$, and the **Ir1** to **Ir3** complexes were obtained from the reaction between the dimeric iridium complexes and the alkyl chain decorated bipyridine (N^N) ligand. The structures of some ligands and final products were characterized by ^{1}H-nuclear magnetic resonance (^{1}H-NMR) and high resolution-mass spectrometry (HR-MS) (Fig. S2–S9†), and the result showed that the synthesized structures were in line with its design.

Optical properties

The absorption spectra of **Ir1**, **Ir2**, **Ir3** in CH_2Cl_2 were shown in Fig. 1a. Variable concentration experiments confirmed that no ground state aggregation occurred in the concentration range from 5 to 50 μM (Fig. S10–S12†). Three Ir(III) complexes exhibited a wide absorption band from UV to visible region. The absorption band below 350 nm was due to the $^1\pi,\pi^*$ transition of C^N and N^N ligands. The absorption band from 350 to 450 nm was due to the $^1\pi,\pi^*$ transition and spin allowed singlet metal to ligand charge transfer (^{1}MLCT) mixed with some singlet ligand to ligand charge transfer (^{1}LLCT) and singlet intra-ligand charge transfer (^{1}ILCT). The absorption band larger than 450 nm was due to the ^{1}MLCT/^{1}LLCT. Especially, three Ir(III) complexes had obvious absorption at 532 nm, the molar absorption coefficients were 2225, 4686, and 2425 L mol^{-1} cm^{-1}, for **Ir1** to **Ir3** respectively, beneficiating to the PDT induced by green light (532 nm).

The emission spectra of **Ir1**, **Ir2**, **Ir3** in CH_2Cl_2 were shown in Fig. 1b. Variable concentration experiments confirmed that no quenching emission intensity occurred from 5 to 50 μM (Fig. S10–S12†). Upon excitation at 532 nm, **Ir1** exhibited major photoluminescence peaks at 636 nm, **Ir2** exhibited major photoluminescence peaks at 778 nm and 855 nm, and **Ir3** exhibited major photoluminescence peaks at 650 nm. Compared to **Ir1**, the **Ir2** showed a red-shifted emission peak and the emission peak located in the near-infrared (NIR) region, which indicated that increasing the conjugation length of the C^N ligand can significantly redshift the position of the emission peak. This result was in line with the reported phenomenon that the degree of π-conjugation of the C^N ligands impacts the location of emission.[39,40] Further, compared to **Ir1**, **Ir3** exhibited a similar emission location, indicating that increasing the rigidity of the C^N ligand cannot change the location of the Ir(III) complex emission. Due to the long linear alkyl substituents on the N^N ligand, three complexes presented good solubility and could be dissolved in different organic solvents such as toluene, tetrahydrofuran (THF), CH_2Cl_2, CH_3CN, and CH_3OH (Fig. S10–S12†).

Taking the air-sensitive emission, luminous lifetime from nanosecond to microsecond, and large Stokes shift into

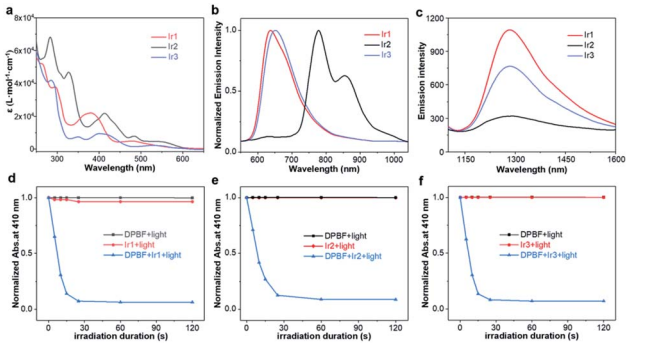

Fig. 1 (a) Absorption and (b) emission spectra of **Ir1**, **Ir2**, and **Ir3** in CH_2Cl_2 (λ_{ex} = 532 nm), (c) $^1O_2$ emission spectra of **Ir1**, **Ir2**, and **Ir3** in CH_3CN (λ_{ex} = 405 nm), time-dependent absorbance plot at 410 nm of (d) **Ir1**, DPBF, and **Ir1** + DPBF, (e) **Ir2**, DPBF, and **Ir2** + DPBF, (f) **Ir3**, DPBF, and **Ir3** + DPBF in CH_3CN (λ_{ex} = 532 nm, 50 mW cm^{-2}).

consideration (Fig. S13–S15, Table S1†), we confirmed that the emission of these complexes was phosphorescence. Then, the position of the phosphorescence emission peak and the luminescence quantum efficiency did not show regular changes with the increase of solvent polarity. Based on these considerations, the emission of **Ir1** to **Ir3** was ascribed to the triplet metal to ligand charge transfer (^{3}MLCT) mixed with triplet ligand to ligand charge transfer (^{3}LLCT). The study of these optical properties showed that the luminescence of these complexes could be applied for cell phosphorescence imaging (Table 1).

Singlet oxygen generation evaluation

Based on the ROS generation mechanism, the triplet excited state lifetime (τ_T) of the Ir(III) complex is a key factor in the generation of $^1O_2$. The longer the triply excited-state lifetime, the more beneficial it is to increase the probability of the complex colliding with oxygen. The transient absorption (TA) spectra of **Ir1**, **Ir2**, and **Ir3** in degassed CH_3CN were shown in Fig. S16.† The τ_T of **Ir1** to **Ir3** were 336 ns, 144 ns, and 309 ns at the maximum triple excited absorption wavelength of 430 nm, 510 nm, and 460 nm, respectively, indicating **Ir1** qualified the longest τ_T. Then, two ways were utilized to evaluate the $^1O_2$ generation ability of three complexes.

First, $^1O_2$ presented the unique emission at 1270 nm. In Fig. 1c, we monitored the unique emission of $^1O_2$ for three complexes. Through 405 nm light excitation, the $^1O_2$ emission at 1270 nm of **Ir1**, **Ir2**, and **Ir3** in CH_3CN was observed, and the luminescence intensity trend of $^1O_2$ was **Ir1** > **Ir3** > **Ir2**, indicating three complexes could catalyze the production of $^1O_2$, and **Ir1** had the highest catalytic efficiency. Subsequently, 1,3-disphenylisobenzofuran (DPBF) as a $^1O_2$ trap could observe the rate of $^1O_2$ production and calculate the singlet oxygen quantum yield (Φ_Δ). In Fig. 1d–f, under the irradiation of 532 nm light, when DPBF was mixed with the solutions of the three complexes, the absorption at 410 nm decreased rapidly with the extension of the irradiation time, and the absorption decreased dramatically within 30 s. After the DPBF solution and the complex solution alone were irradiated with light, almost no decrease in absorbance was observed. This showed that the three complexes could quickly catalyze oxygen to produce $^1O_2$, and the catalytic rate was fast. Furthermore, the singlet oxygen quantum yields of **Ir1** to **Ir3** complexes were calculated to be 0.84, 0.27, and 0.64 respectively (Fig. S17†). Similarly, **Ir1** showed the highest singlet oxygen quantum yield. All of these indicated that **Ir1** qualified the remarkable $^1O_2$ generation performance, and also revealed that increasing the conjugation length of the C^N ligand or increasing its planar rigidity cannot effectively increase the singlet oxygen quantum yield.

Fabrication and characterization of Ir1@BSA to Ir3@BSA

Next, to improve biocompatibility, these iridium complexes were self-assembled with BSA to form nano-photosensitizers by an emulsify method. To weaken the electrostatic interaction by adjusting the pH of the aqueous solution to make BSA around the isoelectric point, these iridium complexes could be well encapsulated with BSA through hydrophobic–hydrophobic interaction. The structures of **Ir1**@BSA to **Ir3**@BSA were characterized by transmission electron microscope (TEM). In Fig. 2a–c, many monodisperse balls were observed in the TEM images. The particle size statistics showed that the particle sizes of the three nano-photosensitizers were 61.1 ± 9.7 nm, 68.5 ± 9.1 nm, and 56.6 ± 8.7 nm for **Ir1**@BSA to **Ir3**@BSA, respectively. This showed that the emulsification method was a general encapsulation method, and the prepared nanomaterials have similar particle sizes. In Fig. 2d–f, dynamic light scattering (DLS) results showed larger hydration particle sizes and the sizes were 135.7 nm, 148.6 nm, and 151.2 nm for **Ir1**@BSA to **Ir3**@BSA, respectively, which was due to the formation of a hydration layer. Furthermore, we analyzed the stability of **Ir1**@BSA to **Ir3**@BSA by hydrated particle size. The results showed that the hydrated particle size of them did not change significantly after 15 days, which maintained a good nano-shape and showed good nano-stability (Fig. S18†). At last, DPBF was also utilized to measure the $^1O_2$ generation ability of **Ir1**@BSA to **Ir3**@BSA in H_2O. In Fig. 2g–i, similar to the result of **Ir1** to **Ir3**, the absorption of DPBF was sharply decreased when it was mixed with **Ir1**@BSA to **Ir3**@BSA. The calculated $^1O_2$ quantum yields were 0.20, 0.06, and 0.23 in H_2O (Fig. S19†), and the rate of singlet oxygen generation has a linear relationship with the excitation light power and the concentration of the **Ir1**@BSA to **Ir3**@BSA (Fig. S20†). These results showed that the three Ir(III) complexes could still show good $^1O_2$ generation ability after being wrapped by BSA to form nano-photosensitizers.

Cellular uptake and cytotoxicity assay

Benefits to the luminescence properties of iridium complexes, the uptake of nano-photosensitizers by cells could be observed through phosphorescence imaging. The emission of **Ir2**@BSA

Table 1 Photophysical properties of Ir1, Ir2, and Ir3

	λ_{abs}[a]/nm ($\varepsilon/10^4$ L mol^{-1} cm^{-1})	λ_{em}[b]/nm (τ_{em}/ns, Φ_{em})	λ_{T1-Tn}[c]/nm (τ_{TA}/ns)	Φ_Δ[d]
Ir1	295 (3.8), 382 (2.2), 480 (0.49)	636 (817, 0.176)	430 (336)	0.84
Ir2	283 (6.8), 327 (4.7), 413 (2.2), 485 (0.79)	778, 855 (—[e], —)	510 (144)	0.27
Ir3	285 (4.2), 350 (0.74), 400 (0.97), 530 (0.23)	650 (737, 0.182)	460 (309)	0.64

[a] Absorption band maxima and molar extinction coefficients in CH_2Cl_2 at room temperature. [b] Room temperature emission band maxima, lifetime, and quantum yield in CH_2Cl_2 (1×10^{-5} mol L^{-1}). [c] Triplet transient absorption band maxima and lifetime in degassed CH_3CN. [d] Singlet oxygen quantum yield in CH_3CN. [e] Too weak to be measured.

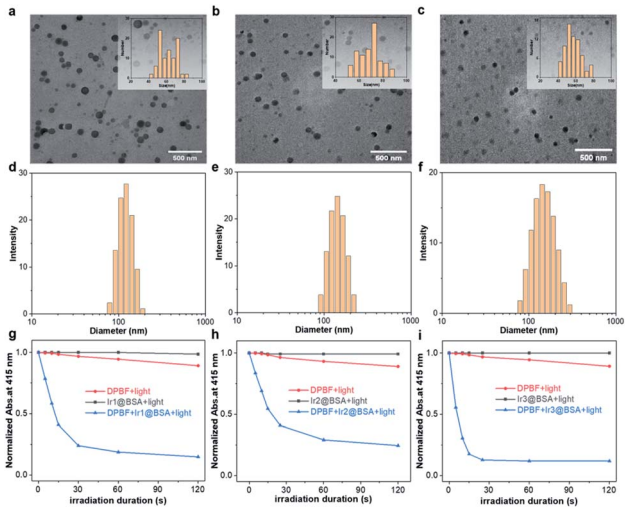

Fig. 2 TEM images of (a) **Ir1**@BSA, (b) **Ir2**@BSA, and (c) **Ir3**@BSA (inset: particle size statistical plot); DLS images of (d) **Ir1**@BSA, (e) **Ir2**@BSA, and (f) **Ir3**@BSA; time-dependent absorption plots at 415 nm of (g) **Ir1**@BSA, DPBF, and **Ir1**@BSA + DPBF, (h) **Ir2**@BSA, DPBF, and **Ir2**@BSA + DPBF, (i) **Ir3**@BSA, DPBF, and **Ir3**@BSA + DPBF in H_2O under 532 nm light irradiation (50 mW cm^{-2}).

located at the NIR region, which exceeded the detection capability of the microscope camera, so we only used cell imaging for **Ir1**@BSA and **Ir3**@BSA to observe their uptake. In Fig. 3, **Ir1**@BSA showed a strong phosphorescence signal in the cytoplasm, and the signal further increased with time, which showed that the uptake of **Ir1**@BSA by cells was good. In comparison, the uptake of **Ir3**@BSA by cells was poor, that is, as the incubation time increased, the fluorescent signal observed in the cells was significantly weaker than **Ir1**@BSA. Further by detecting the content of Ir^{3+} ion in cells, we used the inductively coupled plasma-mass spectrometry (ICP-MS) to detect the uptake of the three nano-photosensitizers in tumor cells. ICP-MS result indicated that the contents of Ir^{3+} ion in cells were 0.95, 0.67, and 0.66 μg g^{-1} for **Ir1**@BSA, **Ir2**@BSA and **Ir3**@BSA respectively, indicating cells had a high uptake rate of **Ir1**@BSA. The difference in the uptake of photosensitizers by cells has a potential impact on the effect of PDT on cells. The mechanism behind this phenomenon is still unclear, and we will study it in our following research.

Afterward, to assess the intracellular light-induced $^1O_2$ production, cell viability was analyzed by Cell Counting Kit-8 (CCK-8) assay in Fig. 4. At a concentration of 40 μM, the cell viability was greater than 90% after cells were incubated with **Ir1**@BSA and **Ir2**@BSA for 24 h, and even at a concentration of 120 μM, the dark toxicity of **Ir3**@BSA was weak, indicating that the dark toxicity of the nano-photosensitizers to cells could be ignored. After exposure to light, we observed different degrees of phototoxicity of cells. As the concentration of nano-photosensitizer increases, **Ir1**@BSA exhibited greater phototoxicity, that is, it has a significant inhibitory effect on cell viability at a lower concentration. The calculated 50% effective concentration (EC_{50}) values of **Ir1**@BSA, **Ir2**@BSA, and **Ir3**@BSA were 5.2 μM, 28.5 μM, and 82.2 μM respectively. The results presented that the efficiency of PDT was **Ir1**@BSA > **Ir2**@BSA > **Ir3**@BSA. The difference in therapeutic effect could be explained by the above-mentioned cellular uptake and singlet oxygen quantum yield. The uptake of **Ir1**@BSA by cells was relatively high, and **Ir1**@BSA showed a remarkable singlet oxygen production rate. Therefore, we believe that the dual roles of **Ir1**@BSA resulted in the best PDT treatment effect.

Live/dead cell staining

The calcein *O*,*O*′-diacetate tetrakis(acetoxymethyl) ester/propidium iodide (calcein-AM/PI) double stain kit was used to directly differentiate the living and dead cells after treatment. In Fig. 5, when mouse breast cancer (4T1) cells were incubated with three nano-photosensitizers without 532 light irradiation, strong green fluorescence emitted from calcein-AM was monitored and the observed red fluorescence emitted from PI was negligible, indicating almost all cells were alive. Further, after the cells were incubated with photosensitizers and irradiated with light, the green fluorescence decreased and the red fluorescence increased, indicating that many cells were dead cells and the three nano-photosensitizers caused different amounts of cell death. The live and dead cell staining consolidated that PDT was effective for 4T1 tumor cell therapy, and **Ir1**@BSA presented the best treatment effect.

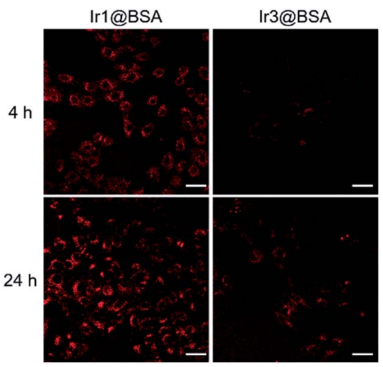

Fig. 3 Luminescence images of 4T1 cells incubated with **Ir1**@BSA or **Ir3**@BSA at 4 h and 24 h. Scale bar, 40 μm.

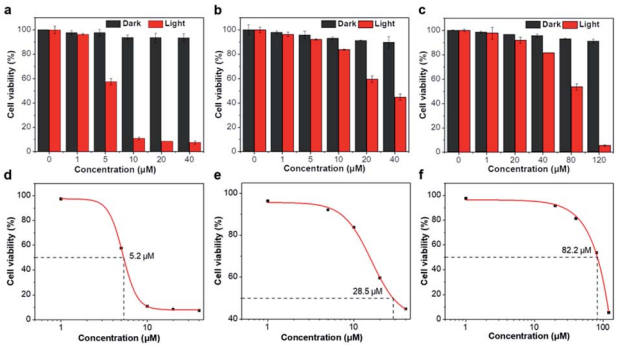

Fig. 4 Cell viability of (a) **Ir1**@BSA, (b) **Ir2**@BSA, and (c) **Ir3**@BSA for 4T1 cells in the dark or 532 nm light irradiation and EC_{50} values of (d) **Ir1**@BSA, (e) **Ir2**@BSA, (f) **Ir3**@BSA under 532 nm light irradiation (100 mW cm^{-2}, 5 min).

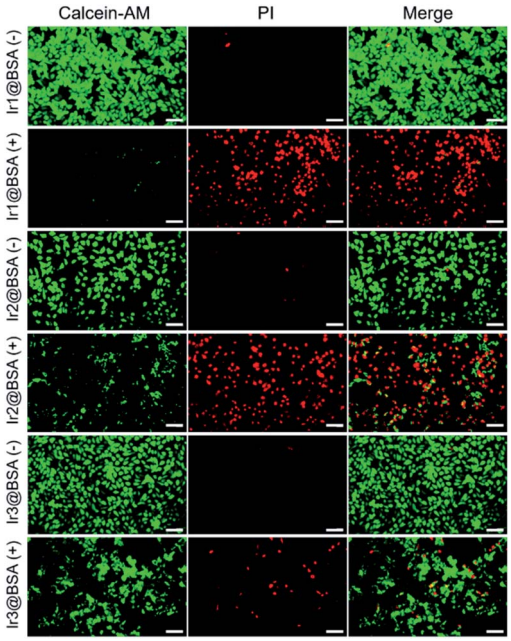

Fig. 5 Fluorescence images of 4T1 cells treated with **Ir1**@BSA to **Ir3**@BSA and then irradiated without (−) or with (+) 532 nm light, and further stained with calcein AM/PI (100 mW cm^{-2}, 5 min). Scale bar, 80 μm.

Intracellular ROS detection

To verify that the production of ROS in cells, 2,7-dichlorodihydrofluorescein diacetate (DCFH-DA) as a cellular ROS indicator could be used to evaluate the $^1O_2$ generation ability of **Ir1**@BSA to **Ir3**@BSA in 4T1 cells. The generated $^1O_2$ could induce DCFH-DA to convert to 2,7-dichlorofluorescein (DCF), which could emit green fluorescence. In Fig. 6, when cells were incubated with **Ir1**@BSA to **Ir3**@BSA respectively, green fluorescence was observed in three group cells after 532 nm light irradiation, while no green fluorescence was monitored in the cells without light irradiation. Through the analysis of the fluorescence intensity, among the three groups of cells exposed to light, the cells incubated with **Ir1**@BSA showed the strongest green fluorescence, indicating that a large amount of ROS was produced in the cells. This further showed that **Ir1**@BSA was an excellent nano-photosensitizer.

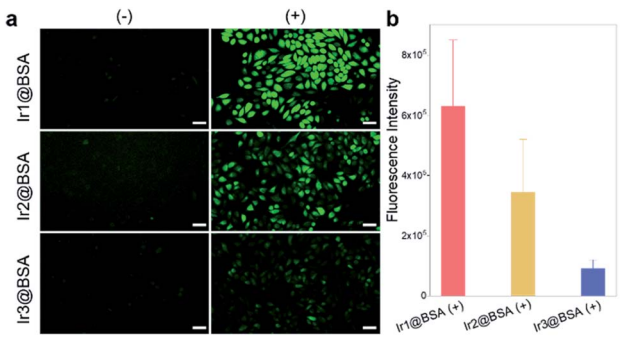

Fig. 6 (a) Fluorescence images of 4T1 cells treated with **Ir1**@BSA to **Ir3**@BSA and then irradiated without (−) or with (+) 532 nm light, and further stained with DCFH-DA (532 nm, 100 mW cm^{-2}, 5 min). Scale bar, 40 μm. (b) The corresponding cell fluorescence quantitative statistical analysis of cells in (a).

Experimental

General

All solvents and reagents used to synthesis were acquired from chemical reagent suppliers, such as Alfa-Aesar, Adamas, Aladdin, and TCI. ^{1}H-NMR spectra were obtained by using a Bruker 400 MHz NMR spectrometer, and the chloroform-d ($CDCl_3$) was used as a solvent. HR-MS spectra were obtained by using an AB SCIEX X500B QTOF electrospray ionization time-of-flight mass spectrometer.

Synthesis procedures

General synthesis procedure of C^N ligand. Corresponding raw materials were added into ethanol (20 mL). The mixture was refluxed for 5 h, then cooled to room temperature (r.t.). Further cooling in the ice bath resulted in a large amount of sediment in the mixture. After filtering by a vacuum pumping and washing with ethanol, it was freeze-dried to obtain corresponding C^N ligand. The crude product is directly used in the next reaction without purification.

dpqx. Raw materials: benzil (420.5 mg, 2 mmol) and benzene-1,2-diamine (216.3 mg, 2 mmol); product: white solid (536 mg, 95%).

dpbq. Raw materials: benzil (420.5 mg, 2 mmol) and naphthalene-2,3-diamine (316.4 mg, 2 mmol); product: bright yellow solid (565 mg, 85%).

dbpz. Raw materials: 9,10-phenanthraquinone (416.4 mg, 2 mmol) and benzene-1,2-diamine (216.3 mg, 2 mmol); product: light yellow solid (527 mg, 94%). ^{1}H-NMR (400 MHz, $CDCl_3$) δ 9.40 (d, $J = 7.9$ Hz, 2H), 8.56 (d, $J = 7.9$ Hz, 2H), 8.37–8.28 (m, 2H), 7.90–7.83 (m, 2H), 7.82–7.71 (m, 4H). HR-MS: m/z calculated for $[C_{20}H_{12}N_2 + H]^+$: 281.1073; found: 281.0991.

General synthesis procedure for dimeric iridium complex. Corresponding raw materials were added into a mixed solvent of 2-methoxyethanol (15 mL) and water (5 mL). The mixture was refluxed under argon protection for 24 h. After cooling to r.t., 5 mL of H_2O was added. Further cooling in the ice bath resulted in precipitate in the mixture. The precipitate was recrystallized with petroleum ether (PE)/CH_2Cl_2 to obtain solid. The solid is directly used in the next reaction without purification.

$[Ir(dpqx)_2]_2Cl_2$. Raw materials: dpqx (124 mg, 0.44 mmol) and $IrCl_3 \cdot xH_2O$ (70 mg, 0.2 mmol); product: red solid (120 mg, 76%).

$[Ir(dpbq)_2]_2Cl_2$. Raw materials: dpbq (146 mg, 0.44 mmol) and $IrCl_3 \cdot xH_2O$ (70 mg, 0.2 mmol); product: dark red solid (128 mg, 72%).

$[Ir(dbpz)_2]_2Cl_2$. Raw materials: dbpz (123 mg, 0.44 mmol) and $IrCl_3 \cdot xH_2O$ (70 mg, 0.2 mmol); product: dark red solid (80 mg, 51%).

General synthesis procedure for Ir1 to Ir3. Corresponding dimeric iridium complex, 4,4′-dinonyl-2,2′-bipyridine (dnbpy),

and silver trifluoromethanesulfonate (F_3CSO_3Ag) were added into a mixed solvent of CH_2Cl_2 (20 mL) and CH_3OH (10 mL). The mixture was refluxed under argon protection for 24 h. After cooling to r.t., NH_4PF_6 (10 equivalent) was added and the mixture was stirred for 1 h. Then, the solvent was removed and the crude product was purified by column chromatography (silica gel, 100–200 mesh; eluent, CH_2Cl_2/ethyl acetate, v/v). The final product was further recrystallized with petroleum ether and CH_2Cl_2.

Ir1. Raw materials: $[Ir(dpqx)_2]_2Cl_2$ (158 mg, 0.1 mmol), dnbpy (81.6 mg, 0.2 mmol), and F_3CSO_3Ag (51.4 mg, 0.2 mmol); column chromatography (100/1, v/v); product: red solid (117 mg, 44.7%). ^{1}H-NMR (400 MHz, $CDCl_3$) δ 8.47 (d, J = 5.7 Hz, 2H), 8.21 (s, 2H), 8.04 (d, J = 0.9 Hz, 1H), 8.02 (d, J = 0.9 Hz, 1H), 7.83 (d, J = 3.9 Hz, 4H), 7.68–7.65 (m, 6H), 7.60 (dd, J = 11.2, 3.9 Hz, 2H), 7.49 (dd, J = 5.7, 1.1 Hz, 2H), 7.36 (s, 1H), 7.34 (s, 1H), 7.18–7.11 (m, 4H), 6.78–6.73 (m, 2H), 6.68 (td, J = 7.5, 1.1 Hz, 2H), 6.47 (d, J = 7.3 Hz, 2H), 2.82 (dd, J = 14.5, 7.3 Hz, 4H), 1.61 (dd, J = 13.6, 7.3 Hz, 4H), 1.26–1.20 (m, 24H), 0.86 (t, J = 6.9 Hz, 6H). HR-MS: m/z calculated for $[C_{68}H_{70}F_6IrN_6P - PF_6]^+$: 1163.5286; found: 1163.5194.

Ir2. Raw materials: $[Ir(dpbq)_2]_2Cl_2$ (178 mg, 0.1 mmol), dnbpy (81.6 mg, 0.2 mmol), and F_3CSO_3Ag (51.4 mg, 0.2 mmol); column chromatography (50/1, v/v); product: dark red solid (174 mg, 61.7%). ^{1}H-NMR (400 MHz, $CDCl_3$) δ 8.63–8.58 (m, 4H), 8.17 (s, 2H), 7.99 (d, J = 8.4 Hz, 2H), 7.91–7.87 (m, 6H), 7.72–7.68 (m, 6H), 7.64 (dd, J = 5.4, 0.8 Hz, 2H), 7.51 (dd, J = 9.7, 4.7 Hz, 2H), 7.42–7.37 (m, 2H), 7.23 (s, 2H), 7.12 (d, J = 8.3 Hz, 2H), 6.78–6.73 (m, 2H), 6.68–6.63 (m, 2H), 6.56 (d, J = 7.1 Hz, 2H), 2.80 (dq, J = 20.6, 6.8 Hz, 4H), 1.64–1.56 (m, 4H), 1.27–1.18 (m, 24H), 0.85 (t, J = 7.0 Hz, 6H). HR-MS: m/z calculated for $[C_{76}H_{74}F_6IrN_6P - PF_6]^+$: 1263.5599; found: 1263.5569.

Ir3. Raw materials: $[Ir(dbpz)_2]_2Cl_2$ (78.6 mg, 0.05 mmol), dnbpy (40.8 mg, 0.1 mmol), and F_3CSO_3Ag (25.7 mg, 0.1 mmol); column chromatography (30/1, v/v); product: dark red solid (53 mg, 40.6%). ^{1}H-NMR (400 MHz, CDCl3) δ 9.45 (d, J = 9.0 Hz, 1H), 8.60 (d, J = 5.1 Hz, 3H), 8.56 (d, J = 8.1 Hz, 1H), 8.39 (d, J = 9.1 Hz, 2H), 8.33 (s, 3H), 8.12 (d, J = 7.9 Hz, 1H), 07.91 (t, J = 7.0 Hz, 2H), 7.86–7.76 (m, 3H), 7.62 (d, J = 5.7 Hz, 1H), 7.29 (d, J = 5.6 Hz, 3H), 7.22 (d, J = 4.4 Hz, 4H), 7.10 (t, J = 7.7 Hz, 2H), 7.02 (d, J = 5.7 Hz, 1H), 6.45 (d, J = 7.5 Hz, 1H), 2.76–2.70 (m, 4H), 1.73–1.69 (m, 4H), 1.33–1.21 (m, 24H), 0.88–0.85 (m, 6H). HR-MS: m/z calculated for $[C_{68}H_{66}F_6IrN_6P - PF_6]^+$: 1159.4973; found: 1159.4961.

Photophysical studies

The UV-vis absorption spectra of **Ir1**, **Ir2**, and **Ir3** in different solvents including toluene, THF, CH_2Cl_2, CH_3CN, and CH_3OH were measured by a UV-1900 spectrometer (Shimadzu, Japan) in a 1 cm quartz cuvette. The emission spectra (λ_{ex} = 436 nm) of **Ir1** and **Ir3** in different solvents were recorded by a fluorescence spectrometer (Edinburgh FS5, UK). The emission spectra of **Ir2** in several solvents were recorded by a fiber optic spectrometer (NOVA-EX, Ideaoptics, China) with a 532 nm laser (China) as an excitation light source. The quantum yields of **Ir1** and **Ir3** were obtained by an FS5 fluorescence spectrometer with an integrating sphere. The emission lifetime was obtained by a flash photolysis spectrometer (Edinburgh LP980, UK) with a 355 nm Nd:YAG laser or a fluorescence spectrometer (FS5) with a 365 nm picosecond laser (Edinburgh, UK).

Singlet oxygen detection

The generated singlet oxygen catalyzed by **Ir1**, **Ir2**, and **Ir3** in CH_3CN was measured by an FS5 fluorescence spectrometer with an InGaAs detector (λ_{ex} = 405 nm). The emission range was recorded from 1100 nm to 1600 nm.

Fabrication and characterization of Ir1@BSA to Ir3@BSA

Ir1 (1.3 mg), **Ir2** (1.4 mg), or **Ir3** (1.3 mg) was dissolved in 1 mL CH_2Cl_2 as an oil phase and BSA (7 mg) was dissolved in 5 mL water (pH = 5) as an aqueous phase. Two phases were emulsified by using an ultrasonic cell crusher (SCIENTZ-950E, China). Afterward, CH_2Cl_2 in the emulsion was removed to obtain a pale orange transparent solution. Finally, the **Ir1**@BSA to **Ir3**@BSA was obtained by filtrating with a mixed cellulose ester membrane filter (pore = 1 μm, Titan, China). The morphology of **Ir1**@BSA to **Ir3**@BSA was observed by a transmission electron microscope (HT7800, Hitachi, Japan). Hydrate particle sizes of **Ir1**@BSA to **Ir3**@BSA in aqueous solution were measured by a laser particle sizer (Malvern Zetasizer Nano ZS90, UK).

Singlet oxygen quantum yield measurement

Singlet oxygen quantum yields (Φ_Δ) of **Ir1** to **Ir3** and **Ir1**@BSA to **Ir3**@BSA were calculated by using a reference method. DPBF was utilized to capture $^1O_2$, and $[Ru(bpy)_3]Cl_2$ was used as a reference (Φ_Δ = 0.56 in CH_3CN).[41] The Φ_Δ of materials depended linearly upon the absorbance degradation rate of DPBF at 410 nm (in CH_3CN) or 415 nm (in H_2O) under the same conditions. In general, DPBF (30 μM) was mixed with **Ir1** to **Ir3** (in CH_3CN) or **Ir1**@BSA to **Ir3**@BSA (in 95% H_2O containing 5% ethanol) in various concentration, then the mixture was irradiated with 532 nm laser. The absorbance at 410 nm or 415 nm was recorded and the Φ_Δ was calculated using the following equation.

$$\Phi_\Delta = \Phi_\Delta^{Ref} \times \frac{W}{W^{Ref}} \times \frac{A^{Ref}}{A} \times \frac{\eta^2}{\eta^{Ref^2}}$$

W is the DPBF degradation rate caused by $^1O_2$, $A = 1 - 10^{-OD}$, A and OD are the absorptivity and absorbance of **Ir1** to **Ir3** or **Ir1**@BSA to **Ir3**@BSA at 532 nm, and η is the refractive index of solvent.[42,43]

Cellular uptake

4T1 cells were seeded in 24-well plates at the density of 1.2×10^4 cells per well and cultured for 24 h (37 °C, 5% CO_2). **Ir1**@BSA or **Ir3**@BSA (20 μM) were added and further incubated for 4 or 24 h. All cells were washed with PBS (pH = 7.4). For imaging method, phosphorescence imaging of cells was recorded by using a CKX41 inverted microscope (Olympus, Japan) with an Olympus U-RFLT50 mercury lamp. A blue light was utilized as an excitation source and the emission was collected in a red

channel. For ICP-MS method, after incubation for 4 h, the cells were collected and digested, and then the content of Ir^{3+} ion was detected by the ICP-MS spectrometer (iCAP™ RQ ICP-MS, Thermo Fisher, USA).

Cytotoxicity assay

4T1 cells were seeded in 96-well plates at the density of 5×10^3 cells per well and cultured for 24 h. Various concentrations of **Ir1**@BSA to **Ir3**@BSA were added into cells and further incubated for 24 h. For dark-toxicity, the cells were washed with PBS. CCK-8 was utilized to evaluate cell viability. The absorbance at 450 nm was recorded by a BioTek Cytation 3 microplate reader (USA). For phototoxicity, after incubation, the cells were irradiated with 532 nm light (100 mW cm^{-2}) for 5 min. After another 24 h incubation, the cells were stained with CCK-8 and the absorbance at 450 nm was measured. The EC_{50} values of phototoxicity were calculated by a sigmoidal fitting of the concentration–cell viability curve.

Live/dead cell staining

Furthermore, a calcein-AM/PI double stain kit was used to stain live and dead cells respectively. The pre-seeded 4T1 cells were incubated with **Ir1**@BSA to **Ir3**@BSA (40 μM) for 24 h, and then cells were irradiated with or without 532 nm irradiation (100 mW cm^{-2}) for 5 min. After another 24 h irradiation, all cells were co-stained with calcein-AM (10 μM) and PI (5 μM) for 30 min and washed with PBS. The fluorescence cell images were collected by an inverted fluorescence microscope (calcein-AM, blue light excitation, green light channel emission; PI, green light excitation, red light channel emission).

Intracellular ROS detection

The fluorescence probe DCFH-DA (Beyotime, China) was used to detect the generation of intracellular ROS. 4T1 cells were seeded in 24-well plates at the density of 1.2×10^4 cells per well and cultured for 24 h. **Ir1**@BSA to **Ir3**@BSA (40 μM) was added and further incubated with cells for 24 h. Subsequently, the cells were washed with PBS and further incubated with DCFH-DA (10 μM) for 30 min. After washing with PBS, cells were irradiated with a 532 nm light (100 mW cm^{-2}) for 5 min. The intracellular fluorescence was recorded immediately by using a CKX41 inverted microscope. The fluorescence intensity was calculated by the cell fluorescence quantitative method *via* ImageJ software.

Conclusions

In summary, we have synthesized and characterized three cyclometalated Ir(III) complexes **Ir1**, **Ir2**, and **Ir3**, and fabricated them with BSA to form nano-photosensitizers **Ir1**@BSA, **Ir2**@BSA, and **Ir3**@BSA for PDT of tumor cells. The results of photophysical studies show that the three iridium complexes have absorption in the UV to the visible light region and phosphorescent emission in the visible light region to the NIR region. Singlet oxygen can be generated after 532 nm light irradiation, and the ability to generate singlet oxygen is **Ir1** > **Ir3** > **Ir2**. Structure–activity relationship studies have shown that extending the conjugation length or increasing the plane rigidity of C^N ligands cannot effectively increase the production of singlet oxygen. After further encapsulation by BSA, **Ir1** to **Ir3** can self-assemble to form nanostructures, which are spherical-like and well dispersed. The diameters are between 50–70 nm and have a stable nano-morphology. After forming the nano-photosensitizers, the singlet oxygen quantum yields of the **Ir1**@BSA, **Ir2**@BSA, and **Ir3**@BSA were 0.20, 0.06, and 0.23 in H_2O, respectively. According to CCK-8 analysis, the three nano-photosensitizers have lower dark toxicity and stronger phototoxicity. The EC_{50} values are 5.2 μM, 28.5 μM, and 82.2 μM for **Ir1**@BSA, **Ir2**@BSA, and **Ir3**@BSA respectively. We attribute this to the dual factors of the difference of cell uptake ability and singlet oxygen generation ability. We furtherly verified the PDT effects of the three nano-photosensitizers with the live/dead cell staining method and the intracellular reactive oxygen staining method, which are consistent with the cell phototoxicity results by the measurement of CCK-8. Therefore, we believe that nano-photosensitizers are different from traditional small-molecule photosensitizers in PDT, which have important significance and value for PDT to increase tumor uptake and biocompatibility in tumor treatment.

Conflicts of interest

There are no conflicts to declare.

Acknowledgements

This work was financially supported by the Natural Science Foundation of Shanghai (19ZR1434700), the National Natural Science Foundation of China (21501121).

Notes and references

1 S. S. Lucky, K. C. Soo and Y. Zhang, Nanoparticles in Photodynamic Therapy, *Chem. Rev.*, 2015, **115**, 1990–2042.
2 K. K. Ng and G. Zheng, Molecular Interactions in Organic Nanoparticles for Phototheranostic Applications, *Chem. Rev.*, 2015, **115**, 11012–11042.
3 M. Wainwright, The problem with dyes in infection control, *Dyes Pigm.*, 2017, **146**, 402–407.
4 C. P. Sabino, M. Wainwright, C. dos Anjos, F. P. Sellera, M. S. Baptista, N. Lincopan and M. S. Ribeiro, Inactivation kinetics and lethal dose analysis of antimicrobial blue light and photodynamic therapy, *Photodiagn. Photodyn. Ther.*, 2019, **28**, 186–191.
5 D. Dolmans, D. Fukumura and R. K. Jain, Photodynamic therapy for cancer, *Nat. Rev. Cancer*, 2003, **3**, 380–387.
6 P. Agostinis, K. Berg, K. A. Cengel, T. H. Foster, A. W. Girotti, S. O. Gollnick, S. M. Hahn, M. R. Hamblin, A. Juzeniene, D. Kessel, M. Korbelik, J. Moan, P. Mroz, D. Nowis, J. Piette, B. C. Wilson and J. Golab, Photodynamic Therapy of Cancer: An Update, *Ca-Cancer J. Clin.*, 2011, **61**, 250–281.
7 J. Jiang, Y. Qian, Z. Xu, Z. Lv, P. Tao, M. Xie, S. Liu, W. Huang and Q. Zhao, Enhancing singlet oxygen generation in

semiconducting polymer nanoparticles through fluorescence resonance energy transfer for tumor treatment, *Chem. Sci.*, 2019, **10**, 5085–5094.

8 L. K. McKenzie, H. E. Bryant and J. A. Weinstein, Transition metal complexes as photosensitisers in one- and two-photon photodynamic therapy, *Coord. Chem. Rev.*, 2019, **379**, 2–29.

9 L. Zhang, Y. Li, W. Che, D. Zhu, G. Li, Z. Xie, N. Song, S. Liu, B. Z. Tang, X. Liu, Z. Su and M. R. Bryce, AIE Multinuclear Ir(III) Complexes for Biocompatible Organic Nanoparticles with Highly Enhanced Photodynamic Performance, *Adv. Sci.*, 2019, **6**, 1802050.

10 J. P. Celli, B. Q. Spring, I. Rizvi, C. L. Evans, K. S. Samkoe, S. Verma, B. W. Pogue and T. Hasan, Imaging and Photodynamic Therapy: Mechanisms, Monitoring, and Optimization, *Chem. Rev.*, 2010, **110**, 2795–2838.

11 S. Ma, J. Zhou, Y. Zhang, B. Yang, Y. He, C. Tian, X. Xu and Z. Gu, An Oxygen Self-sufficient Fluorinated Nanoplatform for Relieved Tumor Hypoxia and Enhanced Photodynamic Therapy of Cancers, *ACS Appl. Mater. Interfaces*, 2019, **11**, 7731–7742.

12 Q. Yu, T. Huang, C. Liu, M. Zhao, M. Xie, G. Li, S. Liu, W. Huang and Q. Zhao, Oxygen self-sufficient NIR-activatable liposomes for tumor hypoxia regulation and photodynamic therapy, *Chem. Sci.*, 2019, **10**, 9091–9098.

13 R. Kv, T.-I. Liu, I. L. Lu, C.-C. Liu, H.-H. Chen, T.-Y. Lu, W.-H. Chiang and H.-C. Chiu, Tumor microenvironment-responsive and oxygen self-sufficient oil droplet nanoparticles for enhanced photothermal/photodynamic combination therapy against hypoxic tumors, *J. Control. Release*, 2020, **328**, 87–99.

14 S.-Z. Ren, B. Wang, X.-H. Zhu, D. Zhu, M. Liu, S.-K. Li, Y.-S. Yang, Z.-C. Wang and H.-L. Zhu, Oxygen Self-Sufficient Core-Shell Metal-Organic Framework-Based Smart Nanoplatform for Enhanced Synergistic Chemotherapy and Photodynamic Therapy, *ACS Appl. Mater. Interfaces*, 2020, **12**, 24662–24674.

15 K. Qiu, M. Ouyang, Y. Liu, H. Huang, C. Liu, Y. Chen, L. Ji and H. Chao, Two-photon photodynamic ablation of tumor cells by mitochondria-targeted iridium(III) complexes in aggregate states, *J. Mater. Chem. B*, 2017, **5**, 5488–5498.

16 L. Wang, H. Yin, P. Cui, M. Hetu, C. Wang, S. Monro, R. D. Schaller, C. G. Cameron, B. Liu, S. Kilina, S. A. McFarland and W. Sun, Near-infrared-emitting heteroleptic cationic iridium complexes derived from 2,3-diphenylbenzo[g]quinoxaline as in vitro theranostic photodynamic therapy agents, *Dalton Trans.*, 2017, **46**, 8091–8103.

17 L. Wang, S. Monro, P. Cui, H. Yin, B. Liu, C. G. Cameron, W. Xu, M. Hetu, A. Fuller, S. Kilina, S. A. McFarland and W. Sun, Heteroleptic Ir(III)N6 Complexes with Long-Lived Triplet Excited States and in Vitro Photobiological Activities, *ACS Appl. Mater. Interfaces*, 2019, **11**, 3629–3644.

18 L. C. Lee, A. W. Tsang, H. W. Liu and K. K. Lo, Photofunctional Cyclometalated Iridium(III) Polypyridine Complexes Bearing a Perfluorobiphenyl Moiety for Bioconjugation, Bioimaging, and Phototherapeutic Applications, *Inorg. Chem.*, 2020, **59**, 14796–14806.

19 V. Novohradsky, A. Rovira, C. Hally, A. Galindo, G. Vigueras, A. Gandioso, M. Svitelova, R. Bresoli-Obach, H. Kostrhunova, L. Markova, J. Kasparkova, S. Nonell, J. Ruiz, V. Brabec and V. Marchan, Towards Novel Photodynamic Anticancer Agents Generating Superoxide Anion Radicals: A Cyclometalated Ir(III) Complex Conjugated to a Far-Red Emitting Coumarin, *Angew. Chem., Int. Ed. Engl.*, 2019, **58**, 6311–6315.

20 Q. Yang, H. Jin, Y. Gao, J. Lin, H. Yang and S. Yang, Photostable Iridium(III)-Cyanine Complex Nanoparticles for Photoacoustic Imaging Guided Near-Infrared Photodynamic Therapy in Vivo, *ACS Appl. Mater. Interfaces*, 2019, **11**, 15417–15425.

21 R. Guan, Y. Chen, L. Zeng, T. W. Rees, C. Jin, J. Huang, Z. S. Chen, L. Ji and H. Chao, Oncosis-inducing cyclometalated iridium(III) complexes, *Chem. Sci.*, 2018, **9**, 5183–5190.

22 M. Lan, S. Zhao, W. Liu, C. S. Lee, W. Zhang and P. Wang, Photosensitizers for Photodynamic Therapy, *Adv. Healthc. Mater.*, 2019, **8**, 1900132.

23 Y. Deng, S. Pan, J. Zheng, Y. Hong, J. Liu, H. Chang, Y. Miao, Y. Sun and Y. Li, Electrostatic self-assembled Iridium(III) nano-photosensitizer for selectively disintegrated and mitochondria targeted photodynamic therapy, *Dyes Pigm.*, 2020, **175**, 108105.

24 H. Lu, X. Jiang, Y. Chen, K. Peng, Y. Huang, H. Zhao, Q. Chen, F. Lv, L. Liu, S. Wang and Y. Ma, Cyclometalated iridium(III) complex nanoparticles for mitochondria-targeted photodynamic therapy, *Nanoscale*, 2020, **12**, 14061–14067.

25 X. Liu, G. Li, M. J. Xie, S. Guo, W. L. Zhao, F. Y. Li, S. J. Liu and Q. Zhao, Rational design of type I photosensitizers based on Ru(II) complexes for effective photodynamic therapy under hypoxia, *Dalton Trans.*, 2020, **49**, 11192–11200.

26 K. Y. Zhang, L. N. Song, T. H. Gu, H. Wang, C. Yang, H. C. Zhou, P. L. Gao, S. J. Liu and Q. Zhao, Cell-Membrane Staining Properties and Photocytotoxicity of a Ruthenium(II) Photosensitizer, *Eur. J. Inorg. Chem.*, 2020, **42**, 3996–4001.

27 H. Su, S. Q. Zhu, M. X. Qu, R. Liu, G. L. Song and H. J. Zhu, 1,3,5-Triazine-Based Pt(II) Metallogel Material: Synthesis, Photophysical Properties, and Optical Power-Limiting Performance, *J. Phys. Chem. C*, 2019, **123**, 15685–15692.

28 S. Q. Zhu, H. Liu, K. Y. Wang, Q. Cheng, Z. X. Ma, R. Liu, G. L. Song and H. J. Zhu, The effects of extended pi-conjugation in bipyridyl ligands on the tunable photophysics, triplet excited state and optical limiting properties of Pt(II) naphthalimidyl acetylide complexes, *Dalton Trans.*, 2019, **48**, 15105–15113.

29 L. H. Zhou, F. F. Wei, J. J. Xiang, H. F. Li, C. B. Li, P. F. Zhang, C. J. Liu, P. Gong, L. T. Cai and K. M. C. Wong, Enhancing the ROS generation ability of a rhodamine-decorated iridium(III) complex by ligand regulation for endoplasmic reticulum-targeted photodynamic therapy, *Chem. Sci.*, 2020, **11**, 12212–12220.

30 J. He, Z. Q. Bai, P. F. Yuan, L. Z. Wu and Q. Liu, Highly Efficient Iridium-Based Photosensitizers for Thia-Paterno-Buchi Reaction and Aza-Photocyclization, *ACS Catal.*, 2021, **11**, 446–455.

31 Y. You and W. Nam, Photofunctional triplet excited states of cyclometalated Ir(III) complexes: beyond electroluminescence, *Chem. Soc. Rev.*, 2012, **41**, 7061–7084.

32 Y. H. Li, N. Dandu, R. Liu, L. Hu, S. Kilina and W. F. Sun, Nonlinear Absorbing Cationic Iridium(III) Complexes Bearing Benzothiazolylfluorene Motif on the Bipyridine (N^N) Ligand: Synthesis, Photophysics and Reverse Saturable Absorption, *ACS Appl. Mater. Interfaces*, 2013, **5**, 6556–6570.

33 Y. H. Li, N. Dandu, R. Liu, Z. J. Li, S. Kilina and W. F. Sun, Effects of Extended π-Conjugation in Phenanthroline (N^N) and Phenylpyridine (C^N) Ligands on the Photophysics and Reverse Saturable Absorption of Cationic Heteroleptic Iridium(III) Complexes, *J. Phys. Chem. C*, 2014, **118**, 6372–6384.

34 Q. Yang, M. Shi, H. Zhao, J. M. Lin, L. An, L. L. Cui, H. Yang, Z. G. Zhou, Q. W. Tian and S. P. Yang, Water-Soluble Polymer Nanoparticles Constructed by Three-Component Self-Assembly: An Efficient Theranostic Agent for Phosphorescent Imaging and Photodynamic Therapy, *Chem.–Eur. J.*, 2017, **23**, 3728–3734.

35 Y. Deng, F. Huang, J. Zhang, J. Liu, B. Li, R. Z. Ouyang, Y. Q. Miao, Y. Sun and Y. H. Li, Dual-light triggered metabolizable nano-micelles for selective tumor-targeted photodynamic/hyperthermia therapy, *Dyes Pigm.*, 2020, **182**, 108105.

36 Y. Deng, X. Wang, Y. T. Liu, Y. Xu, J. Zhang, F. Huang, B. Li, Y. Q. Miao, Y. Sun and Y. H. Li, Dual-light triggered metabolizable nano-micelles for selective tumor-targeted photodynamic/hyperthermia therapy, *Acta Biomater.*, 2021, **119**, 323–336.

37 F. F. Xue, M. Shi, Y. P. Yan, H. Yang, Z. G. Zhou and S. P. Yang, Iridium complex loaded polypyrrole nanoparticles for NIR laser induced photothermal effect and generation of singlet oxygen, *RSC Adv.*, 2016, **6**, 15509–15512.

38 H. J. Xiang, H. Z. Chen, H. J. P. Tham, S. Z. F. Phua, J. G. Liu and Y. L. Zhao, Cyclometalated Iridium(III)-Complex-Based Micelles for Glutathione-Responsive Targeted Chemotherapy and Photodynamic Therapy, *ACS Appl. Mater. Interfaces*, 2017, **9**, 27553–27562.

39 Z. J. Li, P. Cui, C. Z. Wang, S. Kilina and W. F. Sun, Nonlinear Absorbing Cationic Bipyridyl Iridium(III) Complexes Bearing Cyclometalating Ligands with Different Degrees of π-Conjugation: Synthesis, Photophysics, and Reverse Saturable Absorption, *J. Phys. Chem. C*, 2014, **118**, 28764–28775.

40 L. Wang, P. Cui, S. Kilina and W. F. Sun, Toward Broadband Reverse Saturable Absorption: Investigating the Impact of Cyclometalating Ligand π-Conjugation on the Photophysics and Reverse Saturable Absorption of Cationic Heteroleptic Iridium Complexes, *J. Phys. Chem. C*, 2017, **121**, 5719–5730.

41 M. C. DeRosa and R. J. Crutchley, Photosensitized singlet oxygen and its applications, *Coord. Chem. Rev.*, 2002, **233**, 351–371.

42 B. Q. Liu, S. Monro, L. Lystrom, C. G. Cameron, K. Colon, H. M. Yin, S. Kilina, S. A. McFarland and W. F. Sun, Photophysical and Photobiological Properties of Dinuclear Iridium(III) Bis-tridentate Complexes, *Inorg. Chem.*, 2018, **57**, 9859–9872.

43 H. He, S. Ji, Y. He, A. Zhu, Y. Zou, Y. Deng, H. Ke, H. Yang, Y. Zhao, Z. Guo and H. Chen, Photoconversion-Tunable Fluorophore Vesicles for Wavelength-Dependent Photoinduced Cancer Therapy, *Adv. Mater.*, 2017, **29**, 1606690.